Regular Article - Theoretical Physics

Phenomenological discriminations of the Yukawa interactions in two-Higgs doublet models with Z_2 symmetry

Xiao-Dong Cheng[1,2,a], **Ya-Dong Yang**[1,2,b], **Xing-Bo Yuan**[1,2,c]

[1] Institute of Particle Physics, Central China Normal University, Wuhan 430079, Hubei, People's Republic of China
[2] Key Laboratory of Quark and Lepton Physics, Ministry of Education, Wuhan 430079, Hubei, People's Republic of China

Abstract There are four types of two-Higgs doublet models under a discrete Z_2 symmetry imposed to avoid tree-level flavor-changing neutral current, i.e. type-I, type-II, type-X, and type-Y models. We investigate the possibility to discriminate the four models in the light of the flavor physics data, including B_s–$\bar{B}_s$ mixing, $B_{s,d} \rightarrow \mu^+\mu^-$, $B \rightarrow \tau\nu$ and $\bar{B} \rightarrow X_s\gamma$ decays, the recent LHC Higgs data, the direct search for charged Higgs at LEP, and the constraints from perturbative unitarity and vacuum stability. After deriving the combined constraints on the Yukawa interaction parameters, we have shown that the correlation between the mass eigenstate rate asymmetry $A_{\Delta\Gamma}$ of $B_s \rightarrow \mu^+\mu^-$ and the ratio $R = \mathcal{B}(B_s \rightarrow \mu^+\mu^-)_{\text{exp}}/\mathcal{B}(B_s \rightarrow \mu^+\mu^-)_{\text{SM}}$ could be a sensitive probe to discriminate the four models with future precise measurements of the observables in the $B_s \rightarrow \mu^+\mu^-$ decay at LHCb.

1 Introduction

Although the Standard Model (SM) for particle physics has been successful for over three decades, it still shows some problems which solutions could imply physics beyond its scope [1–10]. Recently, the ATLAS [11,12] and CMS [13, 14] experiments at LHC have discovered a new neutral boson with properties consistent with those of the SM Higgs boson [15–20]. With the experimental progress at LHC, it is of great interest to confirm whether this boson is the only one fundamental scalar just as the SM, or belongs to an extended scalar sector responsible to the electroweak symmetry breaking (EWSB). The simplest scenario entertaining

the latter possibility is provided by the two-Higgs doublet models (2HDM).

Besides the SM Higgs sector, an additional Higgs doublet is introduced in the 2HDMs. This class of models can provide new source of CP violation beyond the SM [21], which are needed to explain the observed cosmic matter–antimatter asymmetry. The 2HDMs could also be understood as an effective theory for many natural EWSB scenarios, such as the Minimal Supersymmetric Standard Model (MSSM) [22].

However, unlike the SM, the tree-level flavor-changing neutral current (FCNC) transition in the 2HDM is not forbidden by the Glashow–Iliopoulos–Maiani (GIM) mechanism. These FCNCs can cause severe phenomenological difficulties [23–25]. Besides some other solutions [26–30], this problem can be addressed by imposing a discrete Z_2 symmetry [31]. According to different Z_2 charge assignments, there are four types of 2HDMs, referred to, respectively, as the type-I, type-II, type-X and type-Y 2HDMs [32]. Therefore, phenomenologically distinguishing between these 2HDMs is an important issue and worthy of detailed investigation [33].

The 2HDMs present very interesting phenomena in both low-energy flavor transitions such as $B \rightarrow X_s\gamma$ decay and B_s–$\bar{B}_s$ mixing, and high-energy collider processes such as various Higgs decay channels. At present, many analyses have been performed [34–50], however, most of them concentrate on the type-II 2HDM. In this work, we shall extend the previous analyses and study the possibility to discriminate the four different types of 2HDM in favor of experimental measurement. To constrain the model parameters, we shall consider the following constraints:

- flavor processes: B_s–$\bar{B}_s$ mixing, $\bar{B} \rightarrow X_s\gamma$, $B \rightarrow \tau\nu$ and $B_{s,d} \rightarrow \mu^+\mu^-$ decays,
- direct search for Higgs bosons at LEP, Tevatron, and LHC,
- perturbative unitarity and vacuum stability.

[a] e-mail: chengxd@iopp.ccnu.edu.cn

[b] e-mail: yangyd@mail.ccnu.edu.cn

[c] e-mail: xbyuan@mails.ccnu.edu.cn

For the $B_s \to \mu^+\mu^-$ decay, there are several interesting observables very sensitive to new physics effects as suggested recently by De Bruyn et al. [51]. In this paper, we use these observables to probe the 2HDMs and find the correlation between the mass-eigenstate rate asymmetry $A_{\Delta\Gamma}$ and the ratio $R = \mathcal{B}(B_s \to \mu^+\mu^-)_{\mathrm{exp}}/\mathcal{B}(B_s \to \mu^+\mu^-)_{\mathrm{SM}}$, which could be used to discriminate the four models with future precise measurements of the observables in the $B_s \to \mu^+\mu^-$ decay at LHCb.

Our paper is organized as follows: In the next section, we give a brief review on the 2HDM with the Z_2 symmetry. In Sect. 3, the theoretical formalism for the flavor observables are presented. In Sect. 4, we give our detailed numerical results and discuss the possibility of discriminating the four types of 2HDM. Our conclusions are given in Sect. 5. The relevant Wilson coefficients due to the contributions of 2HDMs are presented in Appendices A and B.

2 2HDM under the Z_2 symmetry

In the 2HDM, the two Higgs doublets Φ_1 and Φ_2 can be generally parameterized as

$$\Phi_i = \begin{pmatrix} \omega_i^+ \\ \frac{1}{\sqrt{2}}(v_i + h_i - iz_i) \end{pmatrix}. \tag{2.1}$$

For a CP-conserving Higgs potential, the two vacuum expectation values (vevs) v_1 and v_2 are real and positive [22]. They satisfy the relations $v_1 = v\cos\beta$ and $v_2 = v\sin\beta$ with $v = 246$ GeV. The physical scalars can be obtained by the rotations

$$\begin{pmatrix} h_1 \\ h_2 \end{pmatrix} = R(\alpha) \begin{pmatrix} H \\ h \end{pmatrix}, \quad \begin{pmatrix} z_1 \\ z_2 \end{pmatrix} = R(\beta) \begin{pmatrix} z \\ A \end{pmatrix},$$

$$\begin{pmatrix} \omega_1^+ \\ \omega_2^+ \end{pmatrix} = R(\beta) \begin{pmatrix} \omega^+ \\ H^+ \end{pmatrix}, \tag{2.2}$$

where the rotation matrix is given by

$$R(\theta) = \begin{pmatrix} \cos\theta & -\sin\theta \\ \sin\theta & \cos\theta \end{pmatrix}. \tag{2.3}$$

The mixing angles α and β are determined by the parameters of the Higgs potential. The physical Higgs spectrum consists of five degrees of freedom: two charged scalars $H^\pm$, two

CP-even neutral scalars h and H, and one CP-odd neutral scalar A.

In the interaction basis, the Yukawa interactions of these Higgs bosons can be written

$$-\mathcal{L}_Y = \bar{Q}_L(Y_1^d\Phi_1 + Y_2^d\Phi_2)d_R + \bar{Q}_L(Y_1^u\tilde{\Phi}_1 + Y_2^u\tilde{\Phi}_2)u_R$$
$$+ \bar{L}_L(Y_1^\ell\Phi_1 + Y_2^\ell\Phi_2)e_R + \mathrm{H.c.}, \tag{2.4}$$

where $\tilde{\Phi}_i = i\sigma_2\Phi_i^*$ with σ_2 the Pauli matrix, Q_L and L_L denote the left-handed quark and lepton doublets, and u_R, d_R, and e_R are the right-handed up-type quark, down-type quark and lepton singlet, respectively. The Yukawa coupling matrices Y_i^f ($f = u, d, \ell$) are 3×3 complex matrices in flavor space.
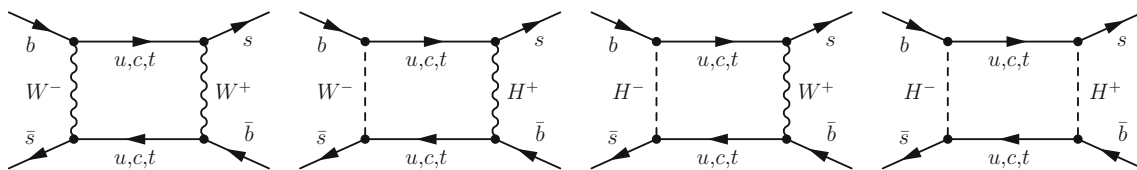
In order to avoid tree-level FCNC, it is natural to introduce a discrete Z_2 symmetry [31]. All the possible nontrivial Z_2 charge assignments are listed in Table 1, which define the four well-known types of 2HDM, i.e. type-I, type-II, type-X and type-Y. The Yukawa interactions in the four models are different. In the mass-eigenstate basis, they can be unified in the form

$$-\mathcal{L}_Y = + \sum_{f=u,d,\ell} \left[m_f\bar{f}f + \left(\frac{m_f}{v}\xi_h^f\bar{f}fh + \frac{m_f}{v}\xi_H^f\bar{f}fH \right. \right.$$
$$\left. \left. -i\frac{m_f}{v}\xi_A^f\bar{f}\gamma_5 fA\right)\right]$$
$$+ \frac{\sqrt{2}}{v}\bar{u}\left(m_uV\xi_A^uP_L + Vm_d\xi_A^dP_R\right)dH^+$$
$$+ \frac{\sqrt{2}m_\ell\xi_A^\ell}{v}\bar{\nu}_L\ell_R H^+ + \mathrm{H.c.}, \tag{2.5}$$

where $P_{L,R} = (1 \pm \gamma_5)/2$ and V denotes the Cabibbo–Kobayashi–Maskawa (CKM) matrix. The couplings $\xi_{h,H,A}^f$ in the four types of 2HDM are listed in Table 2.

Table 1 Charge assignments of the Z_2 symmetry in the four types of 2HDM

	Φ_1	Φ_2	u_R	d_R	ℓ_R	Q_L, L_L
Type-I	$+$	$-$	$-$	$-$	$-$	$+$
Type-II	$+$	$-$	$-$	$+$	$+$	$+$
Type-X	$+$	$-$	$-$	$-$	$+$	$+$
Type-Y	$+$	$-$	$-$	$+$	$-$	$+$

Table 2 Yukawa couplings in the four types of 2HDM

	ξ_h^u	ξ_h^d	ξ_h^ℓ	ξ_H^u	ξ_H^d	ξ_H^ℓ	ξ_A^u	ξ_A^d	ξ_A^ℓ
Type-I	c_α/s_β	$+c_\alpha/s_\beta$	$+c_\alpha/s_\beta$	s_α/s_β	s_α/s_β	s_α/s_β	$-\cot\beta$	$+\cot\beta$	$+\cot\beta$
Type-II	c_α/s_β	$-s_\alpha/c_\beta$	$-s_\alpha/c_\beta$	s_α/s_β	c_α/c_β	c_α/c_β	$-\cot\beta$	$-\tan\beta$	$-\tan\beta$
Type-X	c_α/s_β	$+c_\alpha/s_\beta$	$-s_\alpha/c_\beta$	s_α/s_β	s_α/s_β	c_α/c_β	$-\cot\beta$	$+\cot\beta$	$-\tan\beta$
Type-Y	c_α/s_β	$-s_\alpha/c_\beta$	$+c_\alpha/s_\beta$	s_α/s_β	c_α/c_β	s_α/s_β	$-\cot\beta$	$-\tan\beta$	$+\cot\beta$

Fig. 1 Box diagrams for the $B_s-\bar{B}_s$ mixing in the SM and 2HDM

3 Theoretical formalism for flavor observables

In this section, we shall recapitulate the basic theoretical formulas for the relevant B-meson decay and mixing processes and discuss the contributions of the four types of 2HDMs.

3.1 $B_s-\bar{B}_s$ mixing

For the $B_s-\bar{B}_s$ mixing, the mass difference is defined as
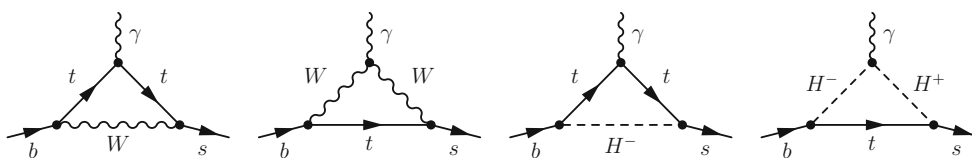
$$\Delta m_{B_s} = m_H - m_L, \tag{3.1}$$

where H and L denote the heavy and light mass eigenstates. This quantity arises from W box diagrams in the SM and can receive contributions from Higgs box diagrams in 2HDM, as shown in Fig. 1. The theoretical prediction can be expressed as [52–54]

$$\Delta m_{B_s} = \frac{G_F^2}{6\pi^2} m_W^2 |V_{tb} V_{ts}^*|^2 S(x_t, x_{H^\pm}) \hat{\eta}_{B_s}$$
$$\times \mathcal{B}_{B_s}(m_b) f_{B_s}^2 m_{B_s}, \tag{3.2}$$

with the definitions $x_t \equiv (\overline{m}_t(\overline{m}_t))^2 / m_W^2$ and $x_{H^\pm} \equiv m_{H^\pm}^2 / m_W^2$. The long-distance QCD effects are contained in the bag factor $\mathcal{B}_{B_s}(m_b)$ and the decay constant f_{B_s} [52]. The short-distance contributions from the SM and 2HDM are encoded in the Inami–Lim function $S(x_t, x_{H^\pm})$, with its explicit expression given in Appendix A, and the QCD correction factor $\hat{\eta}_{B_s}$.

3.2 $\bar{B} \to X_s \gamma$ decay

The effective Hamiltonian for $\bar{B} \to X_s \gamma$ at the scale $\mu_b = \mathcal{O}(m_b)$ is given as follows [55–61]:

$$\mathcal{H}_{\text{eff}} = -\frac{G_F}{\sqrt{2}} V_{ts}^* V_{tb}$$
$$\times \left(\sum_{i=1}^{6} C_i(\mu_b) Q_i + C_{7\gamma}(\mu_b) Q_{7\gamma} + C_{8g}(\mu_b) Q_{8g} \right), \tag{3.3}$$

where Q_{1-6} are the four-fermion operators whose explicit expressions are given in Ref. [58]. The remaining magnetic-penguin operators, which are characteristic for this decay, are defined as

$$Q_{7\gamma} = \frac{e}{8\pi^2} m_b \bar{s}_\alpha \sigma^{\mu\nu} (1+\gamma_5) b_\alpha F_{\mu\nu},$$
$$Q_{8g} = \frac{g_s}{8\pi^2} m_b \bar{s}_\alpha \sigma^{\mu\nu} (1+\gamma_5) T_{\alpha\beta}^a b_\beta G_{\mu\nu}^a, \tag{3.4}$$
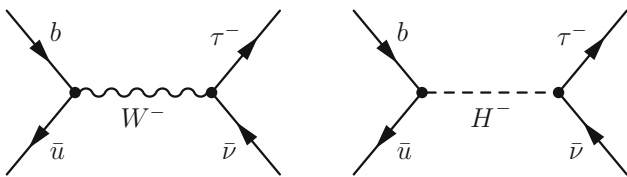
where m_b denotes the b-quark mass in the $\overline{\text{MS}}$ scheme, and e (g_s) is the electromagnetic (strong) coupling constant. The Wilson coefficients $\{C_i\}$ can be calculated perturbatively. In 2HDM, the photon-penguin diagrams mediated by charged Higgs, as shown in Fig. 2, result in the following derivations:

$$C_{7\gamma} = C_{7\gamma}^{\text{SM}} + C_{7\gamma}^{\text{2HDM}}, \qquad C_{8g} = C_{8g}^{\text{SM}} + C_{8g}^{\text{2HDM}}. \tag{3.5}$$

In the SM and the four types of 2HDM, analytic expressions for the Wilson coefficients up to the next-to-leading order (NLO) are given in Refs. [59,60]. The next-to-next-leading order (NNLO) SM and 2HDM calculation can be found in Ref. [62] and Ref. [44], respectively.

The branching ratio of $\bar{B} \to X_s \gamma$ with an energy cut-off E_0 can be expressed as

$$\mathcal{B}(\bar{B} \to X_s \gamma)_{E_\gamma \geq E_0} = \mathcal{B}(\bar{B} \to X_c e \bar{\nu})_{\text{exp}}$$
$$\times \left| \frac{V_{ts}^* V_{tb}}{V_{cb}} \right|^2 \frac{6\alpha_e}{\pi C} [P(E_0) + N(E_0)], \tag{3.6}$$

Fig. 2 One-loop diagrams contributing to $\bar{B} \to X_s \gamma$ through the W boson and the charged Higgs boson exchange in the SM and 2HDM, respectively

Fig. 3 Tree-level diagrams contributing to $B \to \tau \nu_\tau$ in the SM and 2HDM

with the semi-leptonic factor

$$C = \left| \frac{V_{ub}}{V_{cb}} \right|^2 \frac{\Gamma(\bar{B} \to X_c e \bar{\nu})}{\Gamma(\bar{B} \to X_u e \bar{\nu})}. \tag{3.7}$$

The perturbative quantity $P(E_0)$, which is expressed in terms of Wilson coefficients, and the non-perturbative correction $N(E_0)$ can be found in Ref. [59].

3.3 $B \to \tau \nu$ decay

The tauonic decay $B \to \tau \nu$ is described as annihilation processes mediated by W boson in the SM and the charged Higgs boson in 2HDM, as shown in Fig. 3. Therefore, this process is very sensitive to the charged Higgs boson $H^\pm$ and provides an important constraint on the model parameters.

Within 2HDM, the decay width of this channel reads [32,63,64]

$$\Gamma(B \to \tau \nu) = \frac{G_F^2 |V_{ub}|^2}{8\pi} f_B^2 m_B m_\tau^2$$
$$\times \left(1 - \frac{m_\tau^2}{m_B^2}\right)^2 \left(1 - \frac{m_B^2}{m_{H^\pm}^2} \xi_A^d \xi_A^\ell\right)^2, \tag{3.8}$$

where V_{ub} is the CKM matrix element and f_B denotes the B-meson decay constant.

3.4 $B_{s,d} \to \mu^+ \mu^-$ decay

In the SM, the $B_q \to \mu^+ \mu^-$ decays ($q = d$ or s) arise from the W box and Z penguin diagrams at the quark level [65,66],

as shown in Fig. 4. The helicity suppression in these decays may be relaxed by NP contributions, which can significantly enhance their branching ratios. Generally, the low-energy effective Hamiltonian for $B_q \to \mu^+ \mu^-$ decay can be written [67]

$$\mathcal{H}_{\text{eff}} = \frac{G_F}{\sqrt{2}} \frac{\alpha_e}{2\pi s_W} V_{tb}^* V_{tq} (C_S Q_S + C_P Q_P + C_A Q_A), \tag{3.9}$$

with $s_W \equiv \sin \theta_W$. The semi-leptonic operators are defined as

$$Q_S = m_b (\bar{b} P_L q)(\bar{\mu} \mu), \qquad Q_P = m_b (\bar{b} P_L q)(\bar{\mu} \gamma_5 \mu),$$
$$Q_A = (\bar{b} \gamma^\mu P_L q)(\bar{\mu} \gamma_\mu \gamma_5 \mu). \tag{3.10}$$

Among the Wilson coefficients $C_{S,P,A}$, only C_A is non-zero in the SM. Its explicit expressions up to NLO can be found in Refs. [68–70]. Recently, the NLO EW [71] and NNLO QCD [72] corrections have also been completed [73]. In the 2HDM, C_A is not affected, whereas $C_{S,P}$ receive contributions from both charged and neutral Higgs bosons. At present, only the diagrams shown in Fig. 4 have been calculated in the type-II 2HDM with large $\tan \beta$ [67]. Based on these results, we give the Wilson coefficients $C_{S,P}$ corresponding to these diagrams in all the four types of 2HDM with arbitrary $\tan \beta$ in Appendix B. It is noted that contributions from other diagrams may be important for some specific values of $\tan \beta$ (large or small) and will become crucial with future high-precision measurement of $B_q \to \mu^+ \mu^-$ decays.

For $B_q \to \mu^+ \mu^-$ decays, one important observable is the CP averaging branching ratio, which reads

$$\mathcal{B}(B_q \to \mu^+ \mu^-) = \frac{G_F^2 \alpha_e^2}{32\pi^2 s_W^4} \frac{m_{B_q}^3 \tau_{B_q} f_{B_q}^2}{8\pi} \sqrt{1 - \frac{4m_\mu^2}{m_{B_q}^2}}$$
$$\times \left(\frac{2m_\mu}{m_{B_q}}\right)^2 \left| V_{tb} V_{tq}^* \right|^2 |C_A|^2 (|S|^2 + |P|^2), \tag{3.11}$$

Fig. 4 Dominant SM and 2HDM diagrams for the $B_s \to \mu^+ \mu^-$ decays
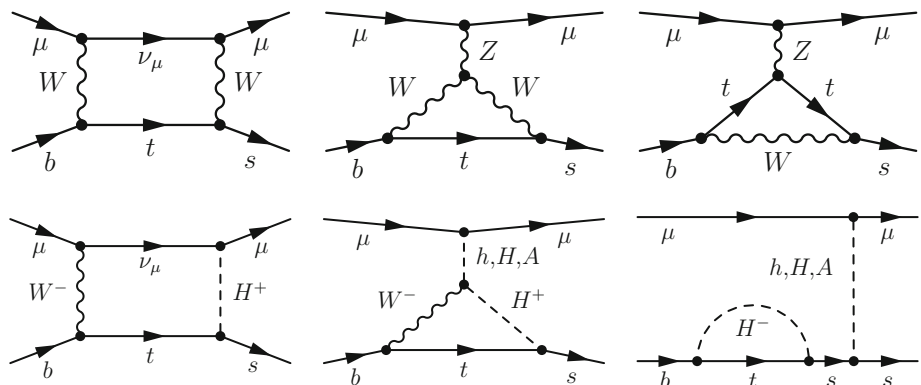
with the definitions

$$P \equiv 1 - \frac{m_{B_q}^2}{2m_\mu} \frac{C_P^*}{C_A^*}, \qquad S \equiv \sqrt{1 - 4\frac{m_\mu^2}{m_{B_q}^2}} \frac{m_{B_q}^2}{2m_\mu} \frac{C_S^*}{C_A^*}. \quad (3.12)$$

It is noted that the contributions of the $C_{S,P}$ terms do not suffer helicity suppression, but they are suppressed by the small leptonic Yukawa coupling in the 2HDMs. However, they may be enhanced by a large $\tan\beta$ (or $\cot\beta$) factor [65–69].

Recently, a sizable width difference $\Delta\Gamma_s$ between the B_s mass eigenstates has been measured at the LHCb [74]

$$y_s \equiv \frac{\Gamma_s^{\mathrm{L}} - \Gamma_s^{\mathrm{H}}}{\Gamma_s^{\mathrm{L}} + \Gamma_s^{\mathrm{H}}} = \frac{\Delta\Gamma_s}{2\Gamma_s} = 0.080 \pm 0.010, \quad (3.13)$$

where Γ_s denotes the inverse of the B_s mean lifetime τ_{B_s}. As pointed out in Ref. [51], the measured branching ratio of $B_q \to \mu^+\mu^-$ should be the time-integrated one, denoted by $\overline{\mathcal{B}}(B_q \to \mu^+\mu^-)$. For $B_s \to \mu^+\mu^-$ decay, in order to compare with the experimental measurement, the sizable width difference effect should be taken into account in the theoretical prediction, and one has

$$\overline{\mathcal{B}}(B_s \to \mu^+\mu^-) = \left[\frac{1 + A_{\Delta\Gamma} y_s}{1 - y_s^2} \right] \mathcal{B}(B_s \to \mu^+\mu^-), \quad (3.14)$$

where $A_{\Delta\Gamma}$ denotes the mass-eigenstate rate asymmetry, which can be expressed as

$$A_{\Delta\Gamma} = \frac{|P|^2 \cos 2\varphi_P - |S|^2 \cos 2\varphi_S}{|P|^2 + |S|^2}, \quad (3.15)$$

where φ_P and φ_S denote the phase of the quantity P and S, respectively. In the four types of 2HDM, $\varphi_P = \varphi_S = 0$. The observable $A_{\Delta\Gamma}$ is complementary to the branching ratio of $B_s \to \mu^+\mu^-$, offering independent information on the short-distance structure of this decay. It can be extracted from the time-dependent untagged decay rate [51,75]. In the SM, $A_{\Delta\Gamma} = +1$. In addition, since the finite width difference in the B_d system is negligible, the approximation $\overline{\mathcal{B}}(B_d \to \mu^+\mu^-) \approx \mathcal{B}(B_d \to \mu^+\mu^-)$ works well.

Following Ref. [51], it is convenient to introduce the ratio

$$R \equiv \frac{\overline{\mathcal{B}}(B_s \to \mu^+\mu^-)}{\mathcal{B}(B_s \to \mu^+\mu^-)_{\mathrm{SM}}} = \frac{1 + y_s \cos 2\varphi_P}{1 - y_s^2}|P|^2$$
$$+ \frac{1 - y_s \cos 2\varphi_S}{1 - y_s^2}|S|^2, \quad (3.16)$$

where $\varphi_P = \varphi_S = 0$ in the four types of 2HDM.

It is also useful to define the following quantity:

$$R_{sd} \equiv \frac{\overline{\mathcal{B}}(B_s \to \mu^+\mu^-)}{\overline{\mathcal{B}}(B_d \to \mu^+\mu^-)}, \quad (3.17)$$

in which some uncertainties of input parameters are canceled out. For example, the f_{B_s}/f_{B_d} in the above ratio can be directly determined by Lattice QCD and the corresponding theoretical uncertainty is significantly reduced [76,77].

4 Numerical analysis and discussions

With the theoretical framework presented in the previous sections, we proceed to present our numerical results and discussion in this section.

4.1 SM predictions and experimental data

4.1.1 Flavor observables within the SM

Within the SM, our predictions for the flavor observables as well as the corresponding experimental data are collected in Table 4. The theoretical uncertainties are obtained by varying the input parameters listed in Table 3 within their respective ranges and adding them in quadrature. It is noted that, taking

Table 3 The relevant input parameters used in the numerical analysis. The meson masses and lifetimes can be found in Ref. [79]

V_{us}	0.22537 ± 0.00063	[78]	s_W^2	0.23116 ± 0.00012	[79]
V_{ub}	$(0.00399 \pm 0.00055)e^{i(-71.1\pm5.1)^\circ}$	[78]	$\alpha_s(m_Z)$	0.1184 ± 0.0007	[79]
V_{cb}	0.04071 ± 0.00096	[78]	$\alpha_e(m_Z)^{-1}$	127.944 ± 0.014	[79]
V_{td}	$(0.00872 \pm 0.00041)e^{i(-24.6\pm2.7)^\circ}$	[78]	f_{B_s}	(227.6 ± 5.0) MeV	[80]
V_{ts}	$(-0.03998 \pm 0.00094)e^{i(1.19\pm0.11)^\circ}$	[78]	f_{B_d}	(190.6 ± 4.7) MeV	[80]
V_{tb}	0.999163 ± 0.000039	[78]	f_{B_s}/f_{B_d}	1.201 ± 0.017	[80]
$\overline{m}_s(\overline{m}_b)$	(0.085 ± 0.017) GeV	[52]	$\mathcal{B}_{B_s}(m_b)$	0.841 ± 0.024	[52]
$\overline{m}_c(\overline{m}_c)$	(1.275 ± 0.025) GeV	[79]	$\hat{\eta}_B$	0.8393 ± 0.0034	[52]
$\overline{m}_b(\overline{m}_b)$	(4.248 ± 0.051) GeV	[52]	$\mathcal{B}(\bar{B} \to X_c e\bar{\nu})$	0.101 ± 0.004	[79]
m_t^{pole}	$(173.5 \pm 0.6 \pm 0.8)$ GeV	[79]	m_b^{1S}	(4.65 ± 0.03) GeV	[79]

Table 4 SM predictions and experimental data for the flavor observables. For the inclusive $\bar{B} \to X_s\gamma$ decay, the value given here corresponds to a photon energy cut at $E_0 = 1.6$ GeV

Observable	SM prediction	Experiment	Ref.
Δm_{B_s} [10^{-11} GeV]	$1.100^{+0.079}_{-0.077}$	1.164 ± 0.005	[79]
$\mathcal{B}(B \to \tau\nu_\tau)$ [10^{-4}]	$1.02^{+0.31}_{-0.27}$	1.65 ± 0.34	[79]
$\mathcal{B}(\bar{B} \to X_s\gamma)$ [10^{-4}]	3.16 ± 0.26	3.43 ± 0.22	[81]
$\bar{\mathcal{B}}(B_d \to \mu^+\mu^-)$ [10^{-10}]	$1.16^{+0.13}_{-0.12}$	$3.6^{+1.6}_{-1.4}$	[82–84]
$\bar{\mathcal{B}}(B_s \to \mu^+\mu^-)$ [10^{-9}]	$3.76^{+0.26}_{-0.25}$	2.9 ± 0.7	[82–84]
R_{sd}	$32.84^{+3.45}_{-3.81}$		
R	1.08 ± 0.01	0.86 ± 0.21	[83,84]

into account the theoretical uncertainties, our SM predictions are in good agreement with the current data. The only tension appears in the branching ratio of $B_d \to \mu^+\mu^-$, which, however, has a rather large experimental error. Thus, strong constraints on the four types of 2HDM and good discrimination between them are excepted.

4.1.2 Direct search for the Higgs bosons

Direct searches for charged Higgs bosons motivated by 2HDM have been performed at LEP [85], Tevatron [86,87] and LHC [88,89]. However, the obtained limits on the charged-Higgs mass depend strongly on the assumed Yukawa structure. In type-II 2HDM, the parameter space with $m_{H^\pm} < m_t$ is almost excluded by the ATLAS [88], which, however, cannot be readily translated into constraints on the parameters of other 2HDMs. Without assumptions on the Yukawa structure, the LEP Collaboration established the bound on the charged Higgs boson mass [85]

$$m_{H^\pm} \geq 79.3 \, \text{GeV},$$

in which $\mathcal{B}(H^+ \to \tau^+\nu_\tau) + \mathcal{B}(H^+ \to c\bar{s}) = 1$ is assumed. In addition, the hadronic $Z \to b\bar{b}$ branching ratio R_b can also set indirect limits on $m_{H^\pm}$. However, the bounds from R_b are weaker than that from the $B_s-\bar{B}_s$ mixing [56].

Recently, the LHC and Tevatron data collected so far [11–14,90] confirm the SM Higgs-like nature [15–20] of the new boson discovered at the LHC, with a spin/parity consistent with the SM 0^+ assignment [91–93]. The observation of its $\gamma\gamma$ decay mode demonstrates that it is a boson with $J \neq 1$, while the $J^P = 0^-$ and 2^+ hypotheses have been already excluded at about 99 % CL, by analyzing the distribution of its decay products. The masses measured by ATLAS and CMS are in good agreement, giving the average value [94]

$$m_h = (125.64 \pm 0.35) \, \text{GeV}.$$

If the light neutral Higgs boson h in 2HDM is identified as the observed resonance at LHC, the decoupling limit $\sin(\beta - \alpha) = 1$ is needed to keep its Yukawa couplings SM-like [48,95,96].

4.1.3 Perturbative unitarity and vacuum stability

Besides the experimental constraints mentioned in previous sections, there are theoretical conditions which allow one to restrict the 2HDM parameter space [22,32,97,98]. The vacuum stability [99] arises from the requirement that the Higgs potential must have a minimum. Perturbative unitarity [100] is the condition that all the (tree-level) scalar–scalar scattering amplitudes must respect unitarity. From these conditions, the following bound can be obtained:

$$|y_t|^2 \leq 4\pi \qquad \text{or} \qquad \tan\beta \geq 0.28,$$

with $|y_t| \equiv (\sqrt{2}\overline{m}_t(m_t^{\text{pole}}))/(v\sin\beta)$ [98].

4.2 Procedure in numerical analysis

As shown in Sect. 2, the relevant 2HDM parameters contain two angles, α and β, and four mass parameters $m_{H^\pm}$, m_h, m_H, and m_A, corresponding to the mass of charged Higgs $H^\pm$, light neutral Higgs h, heavy neutral Higgs H, and CP-odd neutral Higgs A. As discussed in Ref. [95,96], we choose the light neutral Higgs boson h as the observed resonance at LHC and take the decoupling limit $\sin(\beta - \alpha) = 1$. Then the parameter space is reduced to $(m_H, m_A, m_{H^\pm}, \tan\beta)$ and we shall restrict these parameters in the following ranges:

$$m_H \in [m_h, 1000] \, \text{GeV}, \quad m_A \in [1, 1000] \, \text{GeV},$$
$$m_{H^\pm} \in [1, 1000] \, \text{GeV}, \quad \tan\beta \in [0.1, 100].$$

In the numerical analysis, we impose the experimental constraints in the following way: each point in the parameter space corresponds to a theoretical range, constructed from the prediction for the observable in that point together with the corresponding theoretical uncertainty. If this range overlaps with the 2σ range of the experimental measurement, this point is regarded as allowed. In this procedure, to be conservative, the theoretical uncertainty is taken as twice the one listed in Table 4. Since the main theoretical uncertainties arise from hadronic inputs, common to both the SM and the 2HDM, the relative theoretical uncertainty is assumed constant over the parameter space.

4.3 $B_s-\bar{B}_s$ mixing within 2HDM

The mixing parameter Δm_{B_s} is proportional to the Inami–Lim function $S(x_t, x_{H^\pm})$. In the leading order (LO) approximation and taking $m_{H^\pm} = 500$ GeV, we have numerically

Fig. 5 Constraints on the parameter space $(\tan\beta, m_{H^\pm})$ of the four types of 2HDM from Δm_{B_s}. The allowed regions are shown in *black*
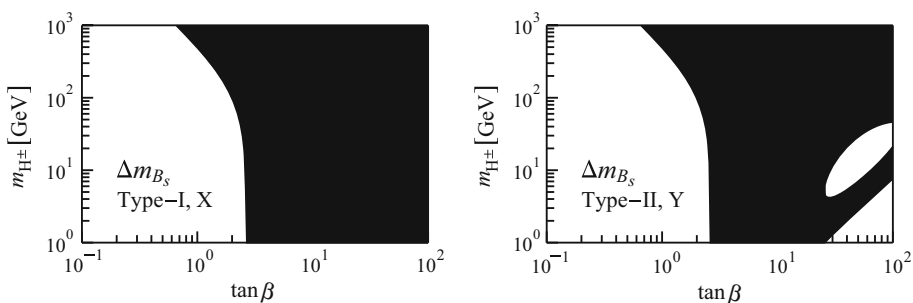
$$\frac{S(x_t, x_{H^\pm})}{S_{\text{SM}}(x_t, x_{H^\pm})}$$
$$= \begin{cases} 1 + \frac{3.5 \times 10^{-2}}{\tan^4\beta} + \frac{0.2}{\tan^2\beta}, & \text{type-I, X,} \\ 1 + \frac{3.5 \times 10^{-2}}{\tan^4\beta} + \frac{0.2}{\tan^2\beta} + 1.6 \times 10^{-6}\tan^2\beta, & \text{type-II, Y.} \end{cases}$$

From these results, we make the following observations:

- For the four different 2HDMs, the dominant effect is proportional to $\cot\beta$. They always work constructively with the SM contribution, even when the charged Higgs mass $m_{H^\pm}$ is not fixed but larger than about 90 GeV.
- Since Δm_{B_s} is only affected by charged Higgs, the contributions from type-I and -X (type-II and -Y) 2HDMs are the same. The type-I and -X Yukawa couplings of down-type quarks are different from the type-II and -Y ones. Thus, there is an additional term proportional to $\tan\beta$ in the latter two 2HDMs, however, suffering from down-type quark mass suppression.

In Fig. 5, the constraints on the parameter space $(\tan\beta, m_{H^\pm})$ from Δm_{B_s} are shown. As expected, the allowed parameter space in type-I, -X 2HDMs and type-II, -Y 2HDMs are almost the same, in which the regions with small $\tan\beta$ are excluded. The difference appears in the region with large $\tan\beta$. However, the allowed charged Higgs mass in this region is below the LEP lower limit.

4.4 $\bar{B} \rightarrow X_s\gamma$ decay within 2HDM

The branching ratio of $\bar{B} \rightarrow X_s\gamma$ decay is proportional to $|C_{7\gamma}^{\text{eff}}(\mu_b)|^2$ in the LO approximation. In 2HDM, the Wilson

coefficient $C_{7\gamma}^{\text{eff}}(\mu_b)$ reads numerically at $m_{H^\pm} = 500$ GeV in the LO,

$$\frac{C_{7\gamma}^{\text{eff}}(\mu_b)}{C_{7\gamma,\text{SM}}^{\text{eff}}(\mu_b)} = \begin{cases} 1 + \frac{0.02}{\tan^2\beta} - \frac{0.18}{\tan^2\beta}, & \text{type-I, X,} \\ 1 + \frac{0.02}{\tan^2\beta} + 0.18, & \text{type-II, Y.} \end{cases}$$

From these numerical results, we make the following observations:

- In the type-I and -X models, the 2HDM effect is proportional to $\cot\beta$ and destructive with the SM contribution.
- In the type-II and -Y models, the 2HDM contribution works constructively with the SM one. Besides the $\tan\beta$ terms, there are also β-independent terms, which dominate the 2HDM contribution for large $\tan\beta$.
- For the $\bar{B} \rightarrow X_s\gamma$, unlike the case of B_s–$\bar{B}_s$ mixing, the dominant operator $Q_{7\gamma}$ is a chirality-flipped operator with the chirality transition $b_R \rightarrow s_L$. Thus the contributions from down-type quark Yukawa couplings do not suffer mass suppression and dominate the ones from up-type quark Yukawa couplings.

In Fig. 6, the constraints on the parameter space $(\tan\beta, m_{H^\pm})$ from $\mathcal{B}(\bar{B} \rightarrow X_s\gamma)$ are shown. The regions with small $\tan\beta$ are largely excluded in all the four types. However, there is still one solution in the type-I and -X 2HDMs, where the destructive interference between the SM and 2HDM contributions makes the coefficient $C_{7\gamma}^{\text{eff}}$ sign-flipped. For the type-II and -Y 2HDMs, the charged Higgs mass is strongly bounded,

Fig. 6 Constraints on the parameter space $(\tan\beta, m_{H^\pm})$ of the four types of 2HDM from $\mathcal{B}(\bar{B} \rightarrow X_s\gamma)$. The allowed regions are shown in *black*
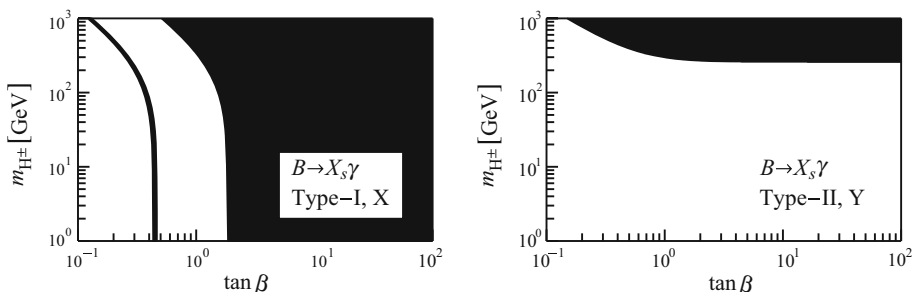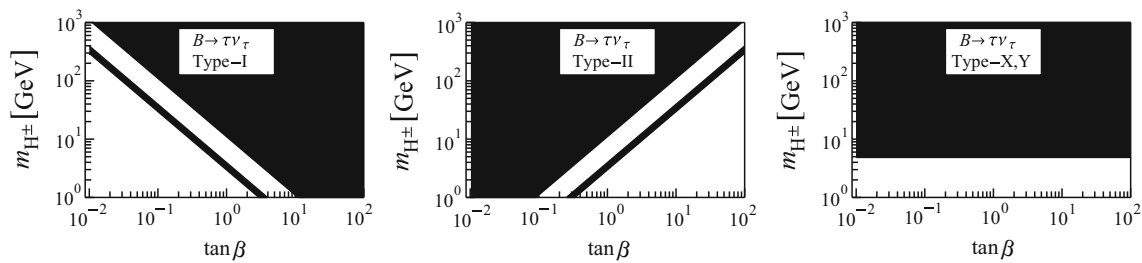
Fig. 7 Constraints on the parameter space ($\tan\beta$, $m_{H^\pm}$) of the four types of 2HDM from $\mathcal{B}(B \to \tau\nu)$. The allowed regions are shown in *black*

$$m_{H^\pm} \geq 259 \, \text{GeV},$$

which mainly arises from the β-independent terms. This lower limit is stronger than the LEP bound.

4.5 $B \to \tau\nu$ decay within 2HDM

For $B \to \tau\nu$ decay, the numerical expressions of the branching ratio read

$$\frac{\mathcal{B}(B \to \tau\nu)}{\mathcal{B}(B \to \tau\nu)_{\text{SM}}}$$
$$= \begin{cases} \left(1 - \frac{27.9}{m_{H^\pm}^2 \tan^2\beta}\right)^2 = (1 - \frac{1.1 \times 10^{-4}}{\tan^2\beta})^2, & \text{type-I,} \\ \left(1 - \frac{27.9 \tan^2\beta}{m_{H^\pm}^2}\right)^2 = (1 - 1.1 \times 10^{-4} \tan^2\beta)^2, & \text{type-II,} \\ \left(1 + \frac{27.9}{m_{H^\pm}^2}\right)^2 = (1 + 1.1 \times 10^{-4})^2, & \text{type-X, Y,} \end{cases}$$

in which the second equality in each line holds for $m_{H^\pm} = 500 \, \text{GeV}$. Here, the 2HDM effects arise from tree-level charged Higgs with leptonic couplings, which make the following features:

- In all the four types, the 2HDM effects are largely suppressed by the charged Higgs mass.
- In the type-II (-I) model, the 2HDM effect is constructive with the SM one and proportional to $\tan\beta$ ($\cot\beta$). The large (small) $\tan\beta$ can compensate the mass suppression.
- In the type-X and -Y model, the 2HDM contribution is β-independent and proportional to $1/m_{H^\pm}$. Thus, a small $m_{H^\pm}$ is expected to be strongly bounded.

The constraints on the parameter space ($\tan\beta$, $m_{H^\pm}$) from $\mathcal{B}(B \to \tau\nu)$ are shown in Fig. 7.[1] As expected, in the type-I (II) 2HDM, excluded regions mainly arise from the parameter space with small (large) $\tan\beta$. There also exists one solution (narrow band in Fig. 7) where the sign of the SM contribution is flipped by the 2HDMs. For the type-X and -Y 2HDMs, a

[1] The bounds derived in this paper are weaker than the ones in the literature, for example in Ref. [40], since a conservative procedure is used in the numerical analysis, which is explained in detail in Sect. 4.2.
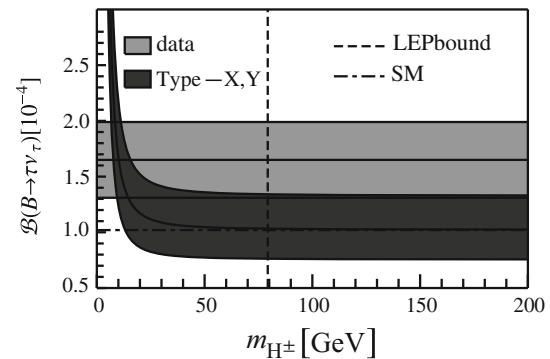
Fig. 8 The type-X and -Y 2HDM predictions on $\mathcal{B}(B \to \tau\nu)$ with the theoretical uncertainty (*dark shaded band*) versus the experimental measurement (*light shaded band*)

β-independent bound on the charged Higgs mass is obtained, $m_{H^\pm} \geq 5 \, \text{GeV}$. However, this lower limit is much weaker than the LEP bound.

Since $\mathcal{B}(B \to \tau\nu)$ is independent of $\tan\beta$ in type-X and type-Y, we also present its theoretical prediction as a function of $m_{H^\pm}$ in Fig. 8, which may be helpful for understanding these two models with reduced experimental and theoretical uncertainties in the future.

4.6 $B_{s,d} \to \mu^+\mu^-$ decays within 2HDM

For $B_s \to \mu^+\mu^-$ decay, taking $m_{H^\pm} = m_H = m_A = 500 \, \text{GeV}$, we get numerically

$$\frac{\overline{\mathcal{B}}(B_s \to \mu^+\mu^-)}{\overline{\mathcal{B}}(B_s \to \mu^+\mu^-)_{\text{SM}}}$$
$$= \begin{cases} 1 - \frac{5.5 \times 10^{-5}}{\tan^2\beta} + \frac{2.5 \times 10^{-4}}{\tan^4\beta} + \frac{4.1 \times 10^{-7}}{\tan^6\beta} + \frac{2.9 \times 10^{-8}}{\tan^8\beta}, & \text{type-I,} \\ 1 + 3.4 \times 10^{-6} - 3.0 \times 10^{-4}\tan^2\beta + 4.3 \times 10^{-8}\tan^4\beta, & \text{type-II,} \\ 1 + 5.5 \times 10^{-5} - \frac{2.5 \times 10^{-4}}{\tan^2\beta} + \frac{3.0 \times 10^{-6}}{\tan^4\beta}, & \text{type-X,} \\ 1 + 3.1 \times 10^{-4}, & \text{type-Y.} \end{cases}$$

Here, both the charged and the neutral Higgs bosons are involved, which results in the following features:

- In all the four types, the 2HDM effects are strongly suppressed by the large mass of CP-even Higgs m_H and
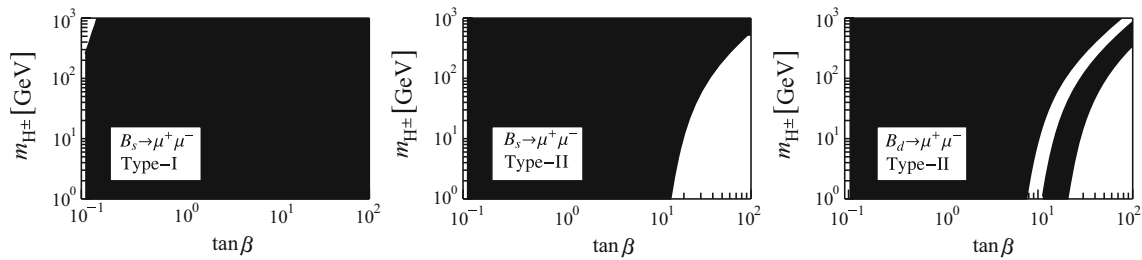
Fig. 9 Constraints on the parameter space of the four types of 2HDM from $\overline{\mathcal{B}}(B_{s,d} \to \mu^+\mu^-)$, plotted in the $\tan\beta$–$m_{H^\pm}$ plane. The allowed regions are shown in *black*

small leptonic Yukawa coupling, and could be enhanced by the small mass of CP-odd Higgs m_A.

- In the type-II (-I and -X) models, the suppressed 2HDM contributions can be compensated by large $\tan\beta$ ($\cot\beta$).
- In the type-Y model, the 2HDM effect is β-independent. However, due to the large suppression, it cannot provide strong bound on the masses of the Higgs bosons.

Under the constraints from $\overline{\mathcal{B}}(B_s \to \mu^+\mu^-)$ and $\overline{\mathcal{B}}(B_d \to \mu^+\mu^-)$, the allowed parameter space (m_H, m_A, $m_{H^\pm}$, $\tan\beta$) of the four types of 2HDM are obtained, which are plotted in the $\tan\beta$–$m_{H^\pm}$ plane in Fig. 9. Due to the large error bars, the current experimental data put almost no constraint on the model parameters, except for the small excluded regions in the type-I and -II 2HDMs.

4.7 Combined analysis and discrimination between the four 2HDMs

Combining all the constraints mentioned in the previous sections, we obtain the surviving parameter space as shown in Fig. 10. From this plot, the following observations are made:

- For small $\tan\beta$, the most stringent constraints come from Δm_{B_s} and $\mathcal{B}(\bar{B} \to X_s\gamma)$ in all the four types of 2HDM.
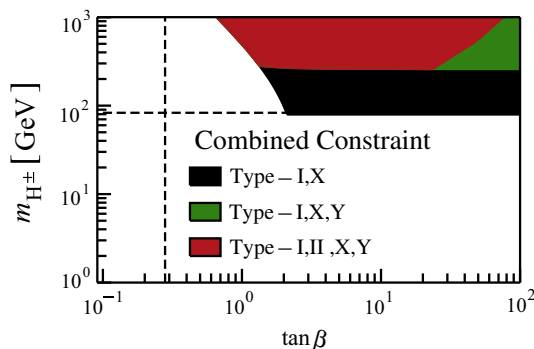
Fig. 10 Combined constraints on the parameter space of the four types of 2HDM, plotted in the $\tan\beta$–$m_{H^\pm}$ plane. The *horizontal dashed line* denotes the direct bound on $m_{H^\pm}$ from the LEP experiment. The *vertical dashed line* denotes the bound on $\tan\beta$ from perturbative unitarity and vacuum stability

- For large $\tan\beta$, the flavor observables put almost no constraints in the type-I and -X models. The LEP bound on $m_{H^\pm}$ is still the most strongest. For type-II and -Y models, the constraints mainly come from $\mathcal{B}(\bar{B} \to X_s\gamma)$. The $B_{s,d} \to \mu^+\mu^-$ decays exclude one additional parameter space of the type-II 2HDM.
- When $m_{H^\pm}$ become large, the combined constraints from flavor observables are almost the same for all the four 2HDMs.
- The allowed region of the type-II model is contained in the one of the type-Y model, which stay in the survived parameter space of the type-I and -X 2HDMs. Therefore, the type-II model can be distinguished from the other 2HDMs in the green region in Fig. 10, and the type-II and -Y models from the other 2HDMs in the black region.

4.8 Other observables in $B_{s,d} \to \mu^+\mu^-$ within 2HDM

At present, only the branching ratio of $B_{s,d} \to \mu^+\mu^-$ have been measured. For the observables $A_{\Delta\Gamma}$ and R defined in Eqs. (3.15) and (3.16), we show in Fig. 11a the correlations between them within the four types of 2HDM, which are obtained in the parameter space given in Sect. 4.7. The 2HDM predictions on R_{sd} defined in Eq. (3.17) are also shown in Fig. 11b. From these plots, we make the following observations:

- For the type-II 2HDM, large derivations from the SM predictions for both $A_{\Delta\Gamma}$ and R are allowed, since both the Wilson coefficients C_S and C_P can be significantly enhanced by large $\tan\beta$. It is also noted that the observable R always decreases.
- For the type-I and -X 2HDMs, only large regions for R are allowed. The reason is that the coefficient C_S cannot be enhanced by small $\tan\beta$, which has been excluded by the combined constraints discussed in Sect. 4.7.
- For the type-Y 2HDM, as expected, its effects on both $A_{\Delta\Gamma}$ and R are small.
- The observables $A_{\Delta\Gamma}$ and R show the potential to discriminate the four types of 2HDM. For the type-I, -II, and -X models, there always exists an allowed region
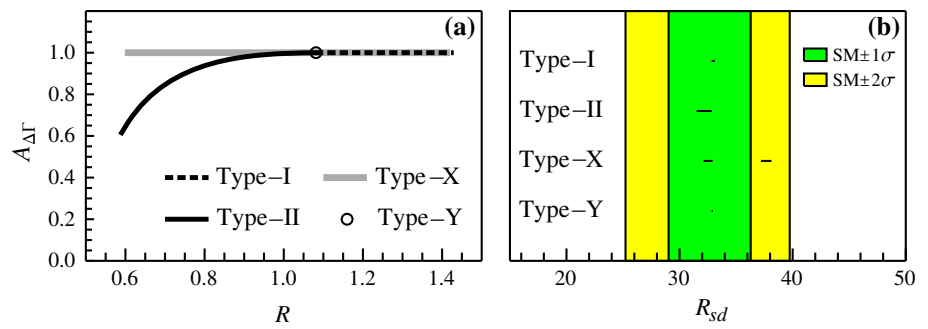
for only one of them in the $R-A_{\Delta\Gamma}$ plane. Interestingly, the allowed region of the type-Y is located in the intersection of the regions of the other 2HDMs. With refined measurement of $A_{\Delta\Gamma}$ and R, one could distinguish one type 2HDM from others, or exclude all the four types.

- At present, due to large uncertainties, the observable R_{sd} cannot provide further information to distinguish between the four 2HDMs. It is also noted that R_{sd} always decreases in the type-II 2HDM.

It is concluded that the observables $A_{\Delta\Gamma}$, R, and R_{sd} in $B_{s,d} \to \mu^+\mu^-$ decays show high sensitivity to the Yukawa structure of the 2HDMs. Improved experimental measurements and theoretical predictions will make these observables more powerful to distinguish between the four types of 2HDM.

5 Conclusions

In this paper, we have studied the possibility to discriminate the four types of 2HDM in the light of recent flavor physics data, including the $B_s-\bar{B}_s$ mixing, the leptonic B-meson decays $B_{s,d} \to \mu^+\mu^-$ and $B \to \tau\nu$, and the inclusive radiative decay $\bar{B} \to X_s\gamma$, together with the experimental data from the direct search for Higgs bosons at LEP, Tevatron and LHC [11–14,85,90] and the constraints from perturbative unitarity [100] and vacuum stability [99]. The outcomes of this combined analysis are summarized as follows:

- The flavor observables exhibit different dependence on the Yukawa couplings in the four types of 2HDMs. With the current experimental data, the allowed region of the type-II model is contained in the one of the type-Y model, which stay in the survived parameter space of the type-I and -X 2HDMs.
- The observables $A_{\Delta\Gamma}$ and R in the $B_s \to \mu^+\mu^-$ decay, which arise from the sizable B_s width difference, are investigated. The correlation between these two observables is found to be sensitive probe to the Yukawa structure of 2HDM.

With the experimental progress expected from the LHC and the future SuperKEKB, as well as the theoretical improvements, the constraints shown here are expected to be refined, which are helpful to discriminate the Yukawa structure if an extended Higgs sector is discovered in the future.

Appendix A: The Inami–Lim function $S(x_t, x_{H^\pm})$

Within the four types of 2HDM discussed in Sect. 2, the Inami–Lim function appearing in $B_s-\bar{B}_s$ mixing is given as [54]

$$S(x_t, x_{H^\pm}) = S_{WW}(x_t) + 2S_{WH}(x_t, x_{H^\pm}) + S_{HH}(x_t, x_{H^\pm}), \tag{A.1}$$

where the basic functions S_{WW} and $S_{WH,HH}$ correspond to the W box and the Higgs box diagrams shown in Fig. 1, respectively. For convenience, their explicit expressions are given here:

$$S_{WW}(x_t)$$
$$= +\left[1 - \frac{11x_t}{4} + \frac{x_t^2}{4} - \frac{3x_t^2 \ln x_t}{2(1-x_t)}\right]\frac{x_t}{(1-x_t)^2}, \tag{A.2}$$

$$2S_{WH}(x_t, x_{H^\pm})$$
$$= +\left[\frac{x_t^2 x_{H^\pm}(x_{H^\pm}-4)}{2(1-x_{H^\pm})(x_t-x_{H^\pm})^2} \ln \frac{x_t}{x_{H^\pm}}\right.$$

$$+ \frac{3x_t^2 \ln x_t}{2(1-x_t)^2(1-x_{H^\pm})} - \frac{x_t^2(4-x_t)}{2(x_{H^\pm}-x_t)(1-x_t)} \Big] (\xi_A^u)^2$$

$$+ \Big[\frac{x_t^2}{(x_{H^\pm}-x_t)^2} \ln \frac{x_{H^\pm}}{x_t} + \frac{x_t}{(x_t-x_{H^\pm})} \Big]$$

$$\times \Big(\frac{1}{12} - \frac{m_{B_s}^2}{2\tilde{m}_{B_s}^2} \Big) 3\sqrt{x_b x_s}(\xi_A^d)^2, \tag{A.3}$$

$$4S_{HH}(x_t, x_{H^\pm})$$

$$= + \Big[\frac{x_{H^\pm}+x_t}{(x_t-x_{H^\pm})^2} + \frac{2x_t x_{H^\pm}}{(x_{H^\pm}-x_t)^3} \ln \frac{x_t}{x_{H^\pm}} \Big] x_t^2 (\xi_A^u)^4$$

$$+ \Big[\frac{x_t^2+x_t x_{H^\pm}}{(x_{H^\pm}-x_t)^2 x_{H^\pm}} + \frac{2x_t^2}{(x_{H^\pm}-x_t)^3} \ln \frac{x_t}{x_{H^\pm}} \Big] x_b x_s (\xi_A^d)^4$$

$$+ \Big[\frac{2}{(x_{H^\pm}-x_t)^2} + \frac{x_t+x_{H^\pm}}{(x_{H^\pm}-x_t)^3} \ln \frac{x_t}{x_{H^\pm}} \Big]$$

$$\times \Big(-\frac{3}{2} + \frac{m_{B_s}^2}{\tilde{m}_{B_s}^2} \Big) x_t^2 \sqrt{x_b x_s}(\xi_A^u \xi_A^d)^2$$

$$+ \Big[\frac{2}{(x_{H^\pm}-x_t)^2} + \frac{x_t+x_{H^\pm}}{(x_{H^\pm}-x_t)^3} \Big] \Big[(x_b+x_s) \frac{5m_{B_s}^2}{2\tilde{m}_{B_s}^2}$$

$$+ \sqrt{x_b x_s} \Big(1 - \frac{6m_{B_s}^2}{\tilde{m}_{B_s}^2} \Big) \Big] x_t^2 (\xi_A^u \xi_A^d)^2, \tag{A.4}$$

with $\tilde{m}_{B_s}^2 \equiv (\overline{m}_b(\overline{m}_b)+\overline{m}_s(\overline{m}_b))^2$ and $x_q \equiv (\overline{m}_q(\overline{m}_b))^2/m_W^2$ for $q=s,b$.

Appendix B: The Wilson coefficients C_S and C_P

Within the four types of 2HDM discussed in Sect. 2, the Wilson coefficients C_S and C_P appearing in the effective Hamiltonian of $B_{s,d} \to \mu^+\mu^-$ are given as [67]

$$C_S = C_S^{\text{box}} + C_S^{\text{peng}} + C_S^{\text{self}},$$
$$C_P = C_P^{\text{box}} + C_P^{\text{peng}} + C_P^{\text{self}}, \tag{B.1}$$

where the functions $C_{S,P}^{\text{box}}$, $C_{S,P}^{\text{peng}}$, and $C_{S,P}^{\text{self}}$ correspond to the box, penguin, and self-energy diagrams associated with Higgs bosons in Fig. 4. Based on the results in Ref. [67], their explicit expressions are given here:

$$C_{S,P}^{\text{box}} = \frac{m_\mu}{2} \frac{\xi_A^\ell \xi_A^d}{m_W^2} B_+(x_{H^\pm}, x_t),$$

$$C_S^{\text{peng}} = \frac{m_\mu}{2} \Big[\frac{\cos(\alpha-\beta)\xi_h^\ell \xi_A^d}{m_h^2} (1-x_{H^\pm}+x_h)$$

$$- \frac{\sin(\beta-\alpha)\xi_H^\ell \xi_A^d}{m_H^2} (1-x_{H^\pm}+x_H) \Big] P_+(x_{H^\pm}, x_t)$$

$$C_P^{\text{peng}} = \frac{m_\mu}{2} \frac{\xi_A^\ell \xi_A^d}{m_A^2} (1-x_{H^\pm}+x_A) P_+(x_{H^\pm}, x_t),$$

$$C_S^{\text{self}} = \frac{m_\mu}{2} \xi_A^u \xi_A^d \Big(\frac{\xi_H^\ell \xi_H^d}{m_H^2} + \frac{\xi_h^\ell \xi_h^d}{m_h^2} \Big) (x_{H^\pm}-1) P_+(x_{H^\pm}, x_t),$$

$$C_P^{\text{self}} = \frac{m_\mu}{2} \xi_A^u \xi_A^d \Big(\frac{\xi_A^\ell \xi_A^d}{m_A^2} \Big) (x_{H^\pm}-1) P_+(x_{H^\pm}, x_t), \tag{B.2}$$

with the functions

$$B_+(x,y) = \frac{y}{x-y} \Big(\frac{\ln y}{y-1} - \frac{\ln x}{x-1} \Big),$$
$$P_+(x,y) = \frac{y}{x-y} \Big(\frac{x\ln x}{x-1} - \frac{y\ln y}{y-1} \Big). \tag{B.3}$$

References

1. S. Weinberg, Phys. Rev. D **13**, 974 (1976)
2. S. Weinberg, Phys. Rev. D **19**, 1277 (1979)
3. E. Gildener, Phys. Rev. D **14**, 1667 (1976)
4. L. Susskind, Phys. Rev. D **20**, 2619 (1979)
5. G. 't Hooft, C. Itzykson, A. Jaffe, H. Lehmann, P.K. Mitter, I.M. Singer, R. Stora, NATO Adv. Study Inst. Ser. B Phys. **59**, pp. 1 (1980)
6. T. Schwetz, M.A. Tortola, J.W.F. Valle, New J. Phys. **10**, 113011 (2008). arXiv:0808.2016 [hep-ph]
7. A.D. Sakharov, Pisma. Zh. Eksp. Teor. Fiz. **5**, 32 (1967)
8. A.D. Sakharov, JETP Lett. **5**, 24 (1967)
9. A.D. Sakharov, Sov. Phys. Usp. **34**, 392 (1991)
10. A.D. Sakharov, Usp. Fiz. Nauk **161**, 61 (1991)
11. G. Aad et al. [ATLAS Collaboration], Phys. Lett. B **716**, 1 (2012). arXiv:1207.7214 [hep-ex]
12. G. Aad et al. [ATLAS Collaboration], Phys. Lett. B **726**, 88 (2013). arXiv:1307.1427 [hep-ex]
13. S. Chatrchyan et al. [CMS Collaboration], Phys. Lett. B **716**, 30 (2012). arXiv:1207.7235 [hep-ex]
14. S. Chatrchyan et al. [CMS Collaboration], JHEP **1306**, 081 (2013). arXiv:1303.4571 [hep-ex]
15. P.W. Higgs, Phys. Rev. Lett. **13**, 508 (1964)
16. P.W. Higgs, Phys. Lett. **12**, 132 (1964)
17. P.W. Higgs, Phys. Rev. **145**, 1156 (1966)
18. F. Englert, R. Brout, Phys. Rev. Lett. **13**, 321 (1964)
19. G.S. Guralnik, C.R. Hagen, T.W.B. Kibble, Phys. Rev. Lett. **13**, 585 (1964)
20. T.W.B. Kibble, Phys. Rev. **155**, 1554 (1967)
21. A. Pilaftsis, Phys. Rev. D **58**, 096010 (1998). hep-ph/9803297
22. G.C. Branco, P.M. Ferreira, L. Lavoura, M.N. Rebelo, M. Sher, J.P. Silva, Phys. Rept. **516**, 1 (2012). arXiv:1106.0034 [hep-ph]
23. B. McWilliams, L.-F. Li, Nucl. Phys. B **179**, 62 (1981)
24. O.U. Shanker, Nucl. Phys. B **206**, 253 (1982)
25. W.-S. Hou, Phys. Lett. B **296**, 179 (1992)
26. R.S. Chivukula, H. Georgi, Phys. Lett. B **188**, 99 (1987)
27. A.J. Buras, P. Gambino, M. Gorbahn, S. Jager, L. Silvestrini, Phys. Lett. B **500**, 161 (2001). hep-ph/0007085
28. G. D'Ambrosio, G.F. Giudice, G. Isidori, A. Strumia, Nucl. Phys. B **645**, 155 (2002). hep-ph/0207036
29. A.V. Manohar, M.B. Wise, Phys. Rev. D **74**, 035009 (2006). hep-ph/0606172
30. A. Pich, P. Tuzon, Phys. Rev. D **80**, 091702 (2009). arXiv:0908.1554 [hep-ph]
31. S.L. Glashow, S. Weinberg, Phys. Rev. D **15**, 1958 (1977)
32. M. Aoki, S. Kanemura, K. Tsumura, K. Yagyu, Phys. Rev. D **80**, 015017 (2009). arXiv:0902.4665 [hep-ph]
33. S.D. Rindani, R. Santos, P. Sharma, JHEP **1311**, 188 (2013). arXiv:1307.1158

34. V.D. Barger, J.L. Hewett, R.J.N. Phillips, Phys. Rev. D **41**, 3421 (1990)
35. J.F. Gunion, H.E. Haber, G.L. Kane, S. Dawson, Front. Phys. **80**, 1 (2000)
36. R.A. Diaz, hep-ph/0212237
37. A. Djouadi, Phys. Rept. **459**, 1 (2008). hep-ph/0503173
38. Z.-j. Xiao, L.-x. Lu, Phys. Rev. D **74**, 034016 (2006). hep-ph/0605076
39. Q. Chang, Y.-D. Yang, Phys. Lett. B **676**, 88 (2009). arXiv:0808.2933 [hep-ph]
40. F. Mahmoudi, O. Stal, Phys. Rev. D **81**, 035016 (2010). arXiv:0907.1791 [hep-ph]
41. S. Kanemura, K. Tsumura, H. Yokoya, Phys. Rev. D **85**, 095001 (2012). arXiv:1201.6489
42. K. Yagyu, arXiv:1204.0424 [hep-ph]
43. M. Jung, X.-Q. Li, A. Pich, JHEP **1210**, 063 (2012). arXiv:1208.1251 [hep-ph]
44. T. Hermann, M. Misiak, M. Steinhauser, JHEP **1211**, 036 (2012). arXiv:1208.2788 [hep-ph]
45. A. Celis, M. Jung, X.-Q. Li, A. Pich, JHEP **1301**, 054 (2013). arXiv:1210.8443 [hep-ph]
46. C.-Y. Chen, S. Dawson, Phys. Rev. D **87**(5), 055016 (2013). arXiv:1301.0309 [hep-ph]
47. B. Grinstein, P. Uttayarat, JHEP **1306**, 094 (2013) [Erratum-ibid. **1309**, 110 (2013)] arXiv:1304.0028 [hep-ph]
48. O. Eberhardt, U. Nierste, M. Wiebusch, JHEP **1307**, 118 (2013). arXiv:1305.1649 [hep-ph]
49. S. Kanemura, K. Tsumura, H. Yokoya, Phys. Rev. D **88**, 055010 (2013). arXiv:1305.5424 [hep-ph]
50. V. Barger, L. L. Everett, H.E. Logan, G. Shaughnessy. arXiv:1307.3676 [hep-ph]
51. K. De Bruyn, R. Fleischer, R. Knegjens, P. Koppenburg, M. Merk, A. Pellegrino, N. Tuning, Phys. Rev. Lett. **109**, 041801 (2012). arXiv:1204.1737 [hep-ph]
52. A. Lenz, U. Nierste, J. Charles, S. Descotes-Genon, A. Jantsch, C. Kaufhold, H. Lacker, S. Monteil et al., Phys. Rev. D **83**, 036004 (2011). arXiv:1008.1593 [hep-ph]
53. A. Lenz, U. Nierste, J. Charles, S. Descotes-Genon, H. Lacker, S. Monteil, V. Niess, S. T'Jampens, Phys. Rev. D **86**, 033008 (2012). arXiv:1203.0238 [hep-ph]
54. J. Urban, F. Krauss, U. Jentschura, G. Soff, Nucl. Phys. B **523**, 40 (1998). hep-ph/9710245
55. X.-Q. Li, Y.-D. Yang, X.-B. Yuan, JHEP **1108**, 075 (2011). arXiv:1105.0364 [hep-ph]
56. O. Deschamps, S. Descotes-Genon, S. Monteil, V. Niess, S. T'Jampens, V. Tisserand, Phys. Rev. D **82**, 073012 (2010). arXiv:0907.5135 [hep-ph]
57. U. Haisch, The inclusive radiative $B \to X_s \gamma$ decay in the standard model, Ph.D. Thesis
58. A.J. Buras. arXiv:1102.5650 [hep-ph]
59. P. Gambino, M. Misiak, Nucl. Phys. B **611**, 338 (2001). hep-ph/0104034
60. M. Ciuchini, G. Degrassi, P. Gambino, G.F. Giudice, Nucl. Phys. B **527**, 21 (1998). hep-ph/9710335
61. M. Misiak, H.M. Asatrian, K. Bieri, M. Czakon, A. Czarnecki, T. Ewerth, A. Ferroglia, P. Gambino et al., Phys. Rev. Lett. **98**, 022002 (2007). hep-ph/0609232
62. M. Misiak, M. Steinhauser, Nucl. Phys. B **683**, 277 (2004). hep-ph/0401041
63. A.G. Akeroyd, C.H. Chen, Phys. Rev. D **75**, 075004 (2007). hep-ph/0701078
64. A.G. Akeroyd, C.H. Chen, S. Recksiegel, Phys. Rev. D **77**, 115018 (2008). arXiv:0803.3517 [hep-ph]
65. C. Bobeth, T. Ewerth, F. Kruger, J. Urban, Phys. Rev. D **64**, 074014 (2001). hep-ph/0104284
66. A.J. Buras, J. Girrbach, D. Guadagnoli, G. Isidori, Eur. Phys. J. C **72**, 2172 (2012). arXiv:1208.0934 [hep-ph]
67. H.E. Logan, U. Nierste, Nucl. Phys. B **586**, 39 (2000). hep-ph/0004139
68. G. Buchalla, A.J. Buras, Nucl. Phys. B **400**, 225 (1993)
69. M. Misiak, J. Urban, Phys. Lett. B **451**, 161 (1999). hep-ph/9901278
70. G. Buchalla, A.J. Buras, Nucl. Phys. B **548**, 309 (1999). hep-ph/9901288
71. C. Bobeth, M. Gorbahn, E. Stamou, Phys. Rev. D **89**, 034023 (2014). arXiv:1311.1348 [hep-ph]
72. T. Hermann, M. Misiak, M. Steinhauser, JHEP **1312**, 097 (2013). arXiv:1311.1347 [hep-ph]
73. C. Bobeth, M. Gorbahn, T. Hermann, M. Misiak, E. Stamou, M. Steinhauser, arXiv:1311.0903 [hep-ph]
74. RAaij et al. [LHCb Collaboration], Phys. Rev. D **87**, 112010 (2013) arXiv:1304.2600 [hep-ex]
75. A.J. Buras, R. Fleischer, J. Girrbach, R. Knegjens, JHEP **1307**, 77 (2013). arXiv:1303.3820 [hep-ph]
76. A. Bazavov et al., Fermilab Lattice and MILC Collaborations. Phys. Rev. D **85**, 114506 (2012). arXiv:1112.3051 [hep-lat]
77. H. Na, C.J. Monahan, C.T.H. Davies, R. Horgan, G.P. Lepage, J. Shigemitsu, Phys. Rev. D **86**, 034506 (2012). arXiv:1202.4914 [hep-lat]
78. [UTfit Collaboration]. http://www.utfit.org/UTfit/ResultsSummer2012PreICHEP
79. J. Beringer et al., Particle Data Group Collaboration. Phys. Rev. D **86**, 010001 (2012)
80. J. Laiho, E. Lunghi, R.S. Van de Water, Phys. Rev. D **81**, 034503 (2010). arXiv:0910.2928 [hep-ph]. http://mypage.iu.edu/elunghi/webpage/LatAves/page7/page7.html
81. Y. Amhis et al. [Heavy Flavor Averaging Group Collaboration], arXiv:1207.1158 [hep-ex]
82. CMS and LHCb Collaborations [CMS and LHCb Collaboration], CMS-PAS-BPH-13-007
83. R. Aaij et al. [LHCb Collaboration], Phys. Rev. Lett. **111**, 101805 (2013). arXiv:1307.5024 [hep-ex]
84. S. Chatrchyan et al. [CMS Collaboration], Phys. Rev. Lett. **111**, 101804 (2013). arXiv:1307.5025 [hep-ex]
85. A. Heister et al. [ALEPH Collaboration], Phys. Lett. B **543**, 1 (2002) hep-ex/0207054
86. A. Abulencia et al. [CDF Collaboration], Phys. Rev. Lett. **96** (2006) 042003. hep-ex/0510065
87. V.M. Abazov et al., D0 Collaboration. Phys. Lett. B **682**, 278 (2009). arXiv:0908.1811 [hep-ex]
88. The ATLAS collaboration, ATLAS-CONF-2013-090
89. S. Chatrchyan et al., CMS Collaboration. JHEP **1207**, 143 (2012). arXiv:1205.5736 [hep-ex]
90. T. Aaltonen et al. [CDF and D0 Collaborations], Phys. Rev. Lett. **109**, 071804 (2012). arXiv:1207.6436 [hep-ex]
91. G.G. Aad et al. [ATLAS Collaboration], Phys. Lett. B **726**, 120 (2013). arXiv:1307.1432 [hep-ex]
92. S. Chatrchyan et al. [CMS Collaboration], Phys. Rev. Lett. **110**, 081803 (2013). arXiv:1212.6639 [hep-ex]
93. [D0 Collaboration], DO-Note-6387-CONF
94. A. Pich, EPJ Web Conf. **60**, 02006 (2013). [arXiv:1307.7700]
95. D. Carmi, A. Falkowski, E. Kuflik, T. Volansky, J. Zupan, JHEP **1210**, 196 (2012). arXiv:1207.1718 [hep-ph]
96. N. Craig, J. Galloway, S. Thomas, arXiv:1305.2424 [hep-ph]
97. S. Chang, S.K. Kang, J.-P. Lee, K.Y. Lee, S.C. Park, J. Song, JHEP **1305**, 075 (2013). arXiv:1210.3439 [hep-ph]
98. S. Kanemura, T. Kasai, Y. Okada, Phys. Lett. B **471**, 182 (1999). hep-ph/9903289
99. M. Sher, Phys. Rept. **179**, 273 (1989)
100. B.W. Lee, C. Quigg, H.B. Thacker, Phys. Rev. D **16**, 1519 (1977)